

Integrated optical multi-ion quantum logic

<https://doi.org/10.1038/s41586-020-2823-6>

Received: 10 March 2020

Accepted: 12 August 2020

Published online: 21 October 2020

 Check for updates
Karan K. Mehta^{1✉}, Chi Zhang¹, Maciej Malinowski¹, Thanh-Long Nguyen¹, Martin Stadler¹ & Jonathan P. Home¹

Practical and useful quantum information processing requires substantial improvements with respect to current systems, both in the error rates of basic operations and in scale. The fundamental qualities of individual trapped-ion¹ qubits are promising for long-term systems², but the optics involved in their precise control are a barrier to scaling³. Planar-fabricated optics integrated within ion-trap devices can make such systems simultaneously more robust and parallelizable, as suggested by previous work with single ions⁴. Here we use scalable optics co-fabricated with a surface-electrode ion trap to achieve high-fidelity multi-ion quantum logic gates, which are often the limiting elements in building up the precise, large-scale entanglement that is essential to quantum computation. Light is efficiently delivered to a trap chip in a cryogenic environment via direct fibre coupling on multiple channels, eliminating the need for beam alignment into vacuum systems and cryostats and lending robustness to vibrations and beam-pointing drifts. This allows us to perform ground-state laser cooling of ion motion and to implement gates generating two-ion entangled states with fidelities greater than 99.3(2) per cent. This work demonstrates hardware that reduces noise and drifts in sensitive quantum logic, and simultaneously offers a route to practical parallelization for high-fidelity quantum processors⁵. Similar devices may also find applications in atom- and ion-based quantum sensing and timekeeping⁶.

Scaling quantum computing systems while continuing to improve operation fidelities over current implementations is the central practical challenge in achieving general, large-scale quantum computation and simulation. The long coherence times and high-fidelity gates of trapped-ion qubits^{7–9} are likely to be valuable in managing overheads associated with quantum error correction¹⁰, while their reliability and predictability as basic quantum systems may assist in preserving performance as complexity grows. However, the bulk optics arranged over metres-long free-space paths typically used for trapped-ion control are a major source of drift and noise, and are furthermore challenging to parallelize, particularly in two-dimensional trap geometries¹¹.

Previous work has demonstrated planar-fabricated nanophotonic waveguides integrated with surface-electrode ion traps that offer advantages over free-space approaches in beam pointing and phase stability, power usage, addressability and parallelizability⁴. However, the free-space input coupling and low efficiencies in the early work (33-dB loss from input to ion) compromised the potential advantages in stability and limited the utility of the delivered light for spin-motion coupling, which is essential for both ground-state cooling of ion motion and multi-qubit quantum logic.

Here we use integrated optics to drive multi-ion entangling quantum logic with fidelities competitive with those in state-of-the-art experiments across qubit platforms. Our experiments leverage efficient interfacing of multiple input fibres to integrated waveguides in a cryogenic ion trap chip (2.4-dB loss at optical wavelength $\lambda = 729$ nm after cooling to 7 K) via direct attachment. We characterize limiting noise sources, finding considerable room for future improvements. The scalability and precision simultaneously afforded with this approach are promising for

the pursuit of large-scale computation and simulation, and we anticipate that similar techniques will find broad application across a range of atom-based technologies.

We designed trap devices with integrated photonics¹² for fabrication in an openly accessible commercial foundry¹³. An optical micrograph of the device studied in this work is shown in Fig. 1. A surface-electrode Paul trap¹⁴ is formed in the top gold layer of a microfabricated chip, and designed to confine ⁴⁰Ca⁺ ions 50 μ m above the surface at the three zones labelled in Fig. 1b. The trapping potential is formed by radiofrequency (RF) and d.c. potentials applied to the electrodes. Light controlling the ions is input to the device via an attached multi-channel fibre V-groove array.

Figure 2a shows the layers comprising the device. A platinum layer forms a ground plane beneath the trap electrodes; this is intended to shield the silicon substrate from the trap RF fields, avoiding modulation of the trap impedance (and hence voltage supplied to the trap and confining potential) during operation that may result from photoconductivity in the silicon¹⁵. This ground layer also assists in shielding ions from mobile charge carriers in the substrate. Between this ground plane layer and the substrate, thin-film silicon nitride (SiN) is patterned to form waveguides and gratings, with structures implemented for wavelengths used for coherent qubit control (729 nm) and repumping (854 nm and 866 nm wavelengths)¹⁶.

A thin 25-nm SiN layer supports a weakly confined mode with mode area matched to a standard single-mode fibre at these wavelengths (Fig. 2b); these waveguides extend to the chip edge to interface to input/output optical fibres. To route light on-chip, power in this mode is coupled to a highly confined mode in a thicker core (consisting of an

¹Department of Physics, Institute for Quantum Electronics, ETH Zürich, Zurich, Switzerland. ✉e-mail: mehtak@phys.ethz.ch

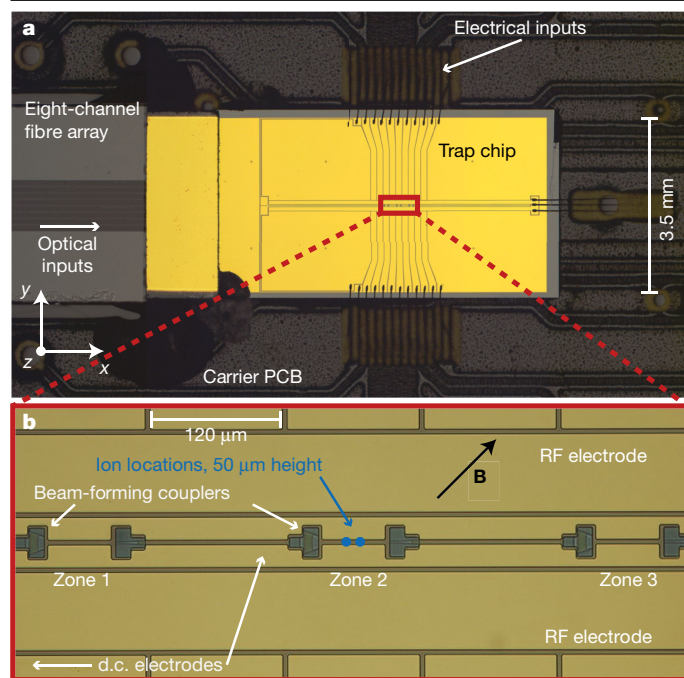


Fig. 1 | Device overview. **a**, Optical micrograph of the assembled ion trap device with an eight-channel fibre array attached; optical fibres extend from the device to a vacuum feedthrough, with optical inputs via standard connectors outside the vacuum chamber. **b**, Higher-magnification view near the trap zones, showing electrode openings for light from waveguide couplers at the three trap zones (zone 3 was used in the experiments presented in this work).

additional 170-nm-thick layer above) via a roughly 1-mm adiabatic taper¹³. These structures allow coupling from multiple attached fibres to on-chip waveguides, with a measured insertion loss of 1.4 dB at room temperature. Fibre feedthroughs on the outer vacuum chamber then allow precise optical delivery to ions in the cryostat by simply connecting optical fibres outside the vacuum chamber. This beam delivery also suppresses noise from beam-pointing fluctuations and cryostat vibrations (Methods).

Input light is routed to the trap zones shown in Fig. 1b, where a waveguide taper expands the lateral mode diameter and a series of curved grating lines serve to emit light into a designed beam. Openings in the trap electrodes transmit the light and are included symmetrically around each trap zone; simulations indicate a negligible impact of these windows on the RF pseudopotential in this design.

Gratings (Fig. 2c) for 729-nm light are designed to uniformly illuminate two ions oriented along the trap axis \hat{x} , and hence focus along \hat{y} and emit a roughly collimated beam along \hat{x} . Grating emission is characterized by scanning the focal plane of a high-numerical-aperture microscope up from the chip surface and capturing a stack of images of the emitted intensity profile at various heights^{4,17} (Methods). Cross-sectional profiles, and the beam profile at the ion trap height of $z = 50 \mu\text{m}$ measured with this method, are shown in Fig. 2c–e.

After the trap die is wirebonded to a carrier printed circuit board (PCB) and the fibre array is attached, the resulting assembly is mounted in a cryogenic vacuum apparatus and cooled to about 7 K for ion-trap experiments. The fibre array is attached in a fashion that allows us to maintain low fibre–chip coupling losses on each channel despite the temperature drop from 300 K (Methods).

Light emitted by the 729-nm couplers drives all transitions between $4S_{1/2}$ and $3D_{5/2}$ with $|\Delta m_j| \leq 2$, where m_j is the secondary total angular momentum quantum number, because the light emitted by the grating couplers contains a mixture of $\hat{\sigma}_+$, $\hat{\sigma}_-$ and $\hat{\pi}$ polarizations relative to the

quantization axis defined by the magnetic field of about 6 G along $\hat{x} + \hat{y}$ (indicated in Fig. 1b). For the experiments below, we choose qubit states $|\downarrow\rangle = |4S_{1/2}, m_j = -1/2\rangle$ and $|\uparrow\rangle = |3D_{5/2}, m_j = -1/2\rangle$, owing to the relatively low differential Zeeman shift (and hence minimal sensitivity to magnetic field fluctuations) of the corresponding transition (0.56 MHz G^{-1}).

In our experiments, two ions are confined in a potential well with axial centre-of-mass (COM) mode frequency $\omega_{\text{COM}} = 2\pi \times 1.2 \text{ MHz}$ (along \hat{x}), with a resulting ion spacing of $5 \mu\text{m}$. Radial mode frequencies are between 3.7 MHz and 5.7 MHz. In each experimental shot, all motional modes are Doppler cooled via conventionally delivered free-space beams, and axial motion is further cooled with electromagnetically induced transparency (EIT) cooling¹⁸. This leaves axial modes with mean phonon numbers $\bar{n} \approx 0.5$, and radial modes with $\bar{n} \approx 5 - 15$. The qubit is prepared in the $|\downarrow\rangle$ state via frequency-selective optical pumping on the $4S_{1/2} \leftrightarrow 3D_{5/2}$ transition with infidelities $< 10^{-4}$ (Methods).

Coherent single-qubit rotations on two ions resulting from a 729-nm pulse resonant with the qubit transition following state preparation and cooling are shown in Fig. 3a. Observed Rabi frequencies are consistent with expectation¹⁹, given this beam profile, power and total loss (6.4 dB input-to-ion; Methods). d.c. potentials are applied to translate ions along \hat{x} to positions where the beam intensity on each ion is equal (Fig. 2f). The observed Rabi oscillations allow us to bound the Rabi frequency imbalance $(1 - \Omega_1/\Omega_2)$ seen by the two ions to $< 1 \times 10^{-2}$. This balancing is sensitive to ion positioning at the level of about 100 nm. The exposed dielectric on the trap surface owing to the grating windows and gaps between electrodes may become charged and generate stray fields that could shift ion positions, but we nevertheless observe that this positioning is stable over hours of experimenting with two-ion chains. The decay in Rabi oscillation amplitude is consistent with that expected given the thermal occupancy of the Doppler-cooled radial modes²⁰.

Ramsey measurements on single ions were performed to assess qubit coherence. With the integrated 729-nm beam path, we observe T_2^* contrast decay times (Extended Data Fig. 3, Methods) that are markedly longer than those observed using the same light addressing the ion through a free-space path. These decays are dominated by phase noise in our 729-nm light. We attribute the enhancement in coherence to the fact that in the free-space configuration, cryostat vibrations relative to the optical table result in laser-phase fluctuation at the ion, a source of noise that is suppressed for the integrated beam path due to the common motion of the grating and trap.

Multi-ion quantum logic gates are commonly mediated by shared motional modes; high-fidelity implementations typically require near-ground-state cooling, particularly of the modes used to enact the gates. We implement gates using axial motion and choose the ‘stretch’ mode in which ions oscillate out of phase (at mode frequency $\omega_{\text{STR}} = \sqrt{3} \omega_{\text{COM}}$), owing to its relative insensitivity to electric (E)-field noise that heats ion motion²¹. We use the light delivered by the integrated couplers to implement pulsed sideband cooling²⁰. Blue sideband flopping following ground-state cooling (Fig. 3b) indicates a mean phonon number in the stretch mode of $\bar{n}_{\text{STR}} \approx 0.05$.

We proceed to implement entangling operations mediated by the ground-state-cooled stretch mode. Mølmer–Sørensen (MS) gates²² apply the unitary $\hat{U}_{\text{MS}}(\phi) = \exp[-i\pi(\sum_k \hat{\sigma}_{\phi,k})^2/8]$, with $\hat{\sigma}_{\phi,k} = \cos\phi \hat{\sigma}_{x,k} + \sin\phi \hat{\sigma}_{y,k}$ representing Pauli operators on qubit k (with $|\uparrow\rangle$ and $|\downarrow\rangle$ the eigenstates of $\hat{\sigma}_z$). The spin phase ϕ is set by laser phases. We implement \hat{U}_{MS} by applying laser light at two frequencies detuned from the stretch mode sidebands of the 729-nm carrier transition at $\omega_{\pm} = \omega_0 \pm (\omega_{\text{STR}} + \delta)$ (Fig. 4). Starting from $|\downarrow\downarrow\rangle$, the ideal implementation generates the Bell state $\frac{1}{\sqrt{2}}(|\downarrow\downarrow\rangle - i|\uparrow\uparrow\rangle)$ after a pulse time of $\tau_g = 2\pi/\delta$. The measured population evolutions as a function of pulse duration are shown in Fig. 4b, together with theoretical predictions for an ideal gate. To measure the coherence of the state produced at $\tau_g = 66 \mu\text{s}$, we apply identical single-qubit rotations

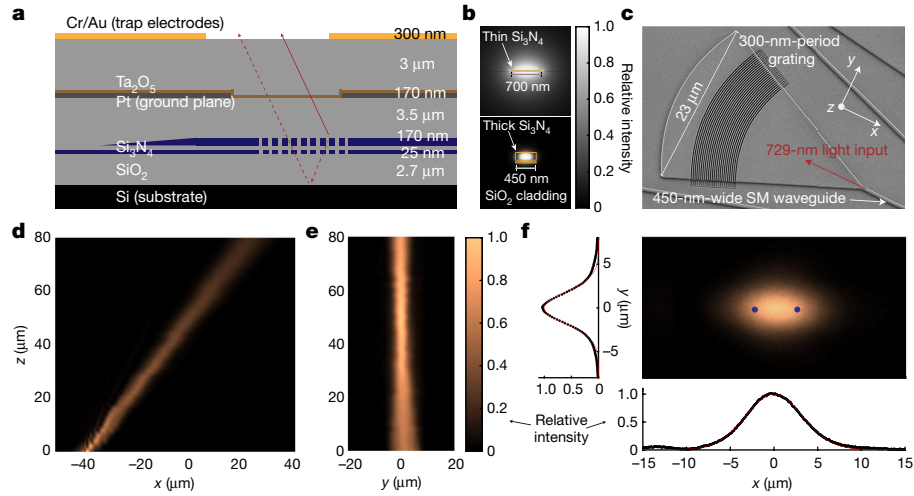


Fig. 2 | Layer stackup and optical design. **a**, Layer stackup in trap fabrication. The top gold layer is patterned to form trap electrodes, to which RF and d.c. potentials are applied to confine ions 50 μm above the surface. The lower platinum serves as a ground plane, and waveguides/gratings are formed in the SiN. The Si substrate is additionally used as a bottom reflector to increase the grating efficiency¹⁷; red arrows represent interfering emission components diffracted directly upwards (solid line) and diffracted downwards and reflected (dashed). **b**, Simulated intensity profiles of quasi-transverse-electric modes (**E** polarized predominantly along the horizontal) of the two waveguide cross-sections, with core areas outlined in gold. **c**, Scanning electron

microscope image of a fabricated grating, showing photolithographically defined waveguides/tapers, and electron-beam-written grating lines with a 300-nm period. SM, single mode. **d, e**, The 729-nm-beam emission profiles in the x - z (**d**) and y - z (**e**) planes, obtained from image stacks of radiated field at various heights z above the trap electrode layer. **f**, Intensity pattern at the trap height $z = 50 \mu\text{m}$; radiation is polarized predominantly along \hat{y} , and Gaussian fits indicate $1/e^2$ intensity radii along the \hat{x} and \hat{y} directions of $w_x = 6.5 \mu\text{m}$ and $w_y = 3.7 \mu\text{m}$, respectively. Blue dots label trapped-ion positions in the radiated beam and confining potential applied.

$\hat{R}_k(\theta, \phi_a) = \exp(-i\theta\hat{\sigma}_{\phi_a,k}/2)$ to both ions ($k = 1, 2$) with $\theta = \pi/2$ after the gate, with variable phase ϕ_a . These ‘analysis’ pulses map the Bell state to states whose parity varies sinusoidally with ϕ_a ; here, parity is defined as $\mathcal{P} = P_{\uparrow\uparrow} + P_{\downarrow\downarrow} - P_{\uparrow\downarrow} - P_{\downarrow\uparrow}$, where the P s are the populations measured in the four possible two-ion outcomes. The contrast of the parity oscillations as a function of ϕ_a is a direct measure of the coherence of the Bell state generated at τ_g (ref. ²³). A maximum-likelihood fit to the data (Fig. 4c) indicates a contrast of 99.2(2)%, with the last-digit uncertainty in parentheses representing the standard deviation of 5,000 bootstrap resamples. Together with the populations measured at the gate time (99.4(1)%, with uncertainty representing 1σ standard error from projection noise), this indicates a total Bell-state fidelity of 99.3(2)%, not correcting for state preparation and measurement error.

Table 1 summarizes the contributing error sources, which are detailed in the Methods. Leading infidelities arise from motional heating and mode-frequency drifts, and laser-frequency noise. Measurements of single-ion heating in our device indicate E -field noise that is about 100 times higher than in other cryogenic planar traps with a similar ion–electrode distance²⁴, suggesting substantial potential for the reduction of this noise. Various technical improvements could reduce motional and laser-frequency drifts in our apparatus; though we have implemented the simplest-possible single-loop gate here, multi-loop and composite-pulse gates can further suppress errors resulting from these drifts²⁵. The only error source fundamental to this choice of qubit is spontaneous emission from the $D_{5/2}$ level, which gives its 1.1-s lifetime contributes an error of 3×10^{-5} for the initial state and 66- μs gate time employed here (this error scales with τ_g).

The infidelities achieved in this work are within an order of magnitude of the lowest demonstrated^{8,9}. While microwave-based schemes are promising for achieving the highest possible fidelities²⁶, we note that the milliwatt-level optical powers in our work are two to three orders of magnitude lower than the powers required in microwave gate implementations in planar traps so far^{27,28}, in which gate times were additionally an order of magnitude longer. Power requirements are likely to be critical in larger-scale systems where dissipation is a concern. The short wavelengths of optical radiation also allow simple

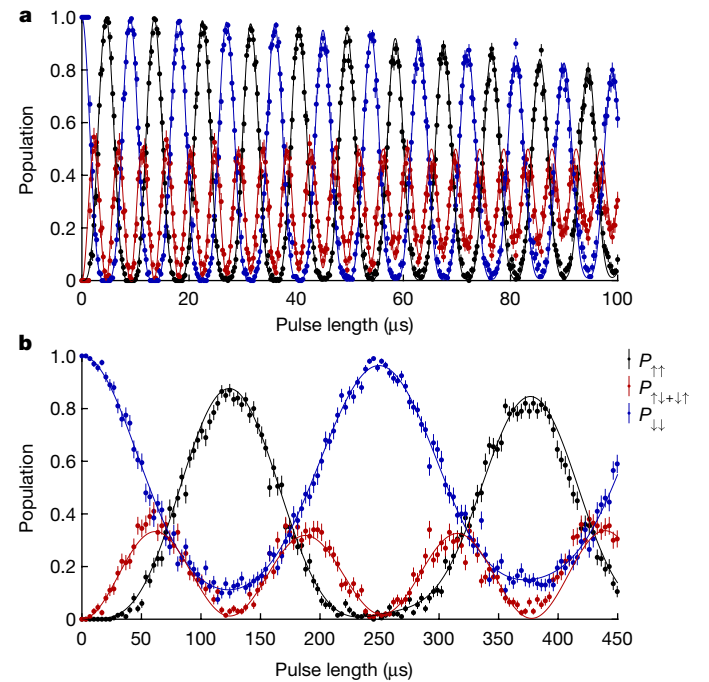


Fig. 3 | Two-ion manipulation and ground-state cooling. **a**, Population evolution versus pulse length under coherent manipulation of two ions with laser frequency ω resonant with the carrier transition at ω_0 . Fits to theory (solid lines) indicate Rabi frequency imbalance between the two ions $< 1 \times 10^{-2}$. **b**, Population evolutions on application of a pulse resonant with the blue sideband ($\omega = \omega_0 + \omega_{\text{STR}}$) on the stretch mode, after sideband cooling with light coupled via the integrated couplers. Lines correspond to theoretical evolutions with $\bar{n}_{\text{STR}} = 0.05$. In both **a** and **b**, each point represents an average over 200 experimental shots, with error bars indicating 1σ standard errors from projection noise.

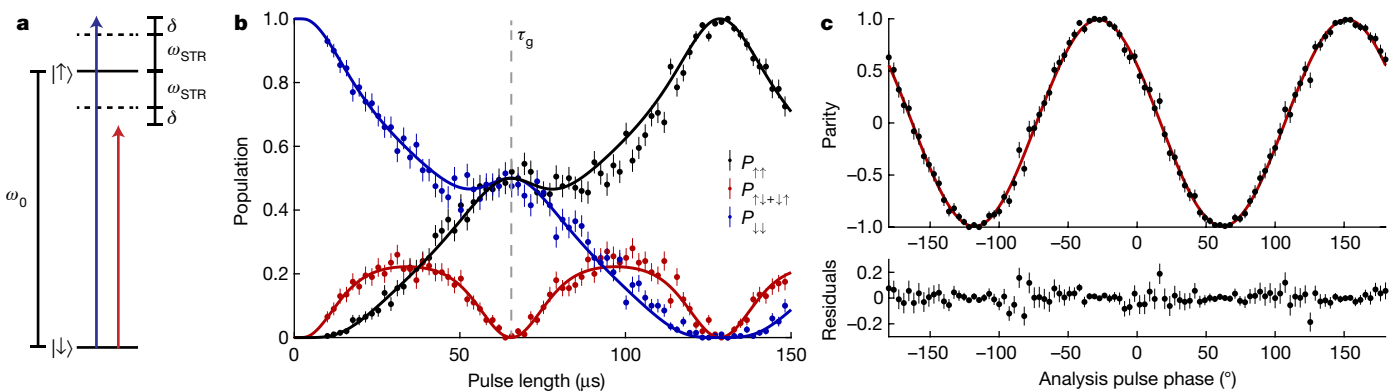


Fig. 4 | Integrated implementation of a two-ion quantum logic gate. **a**, Optical frequencies applied to drive an MS gate; in our experiments $\omega_0 = 2\pi \times 411$ THz (729 nm), $\omega_{\text{STR}} = 2\pi \times 2.0$ MHz and the detuning from motional sidebands is $\delta = 2\pi \times 15$ kHz. **b**, Population evolutions as a function of pulse duration; solid lines show ideal gate evolutions from theory, with gate time as the only free parameter. **c**, Parity oscillations observed on scanning the phase

addressing of particular ions or trap zones^{17,29} without active cancellation. When inputting light to the coupler addressing one zone in the present device, cross-talk at neighbouring zones manifests at the ~ 60 -dB level in relative intensity (Methods). However, spontaneous emission errors and requirements on long-term laser-phase stability may eventually prove problematic in deep quantum circuits; these issues can be alleviated in ions such as $^{40}\text{Ca}^+$ by using both the Zeeman and optical qubit transitions (Methods).

This work motivates developments along multiple fronts. Wavelengths guided in the current chip should allow laser cooling and readout using infrared and high-intensity visible light³⁰, while materials and waveguides for blue/ultraviolet light³¹ allow photoionization, laser cooling and readout at low intensity (recent contemporary work³² demonstrates these functionalities on single-qubit operations, using plasma-enhanced chemical vapour deposition SiN waveguides). This may enable practical, parallel operation of multiple zones with fully integrated beam delivery, in a fashion also extensible to dual-species systems and two-dimensional trap architectures; transport between zones would be a natural step towards large-scale computations^{5,33}. The efficient cryogenic fibre-to-chip coupling shown here, together with stable tight focusing¹⁷, will enable practical, power-efficient fast optical gates³⁴, while combination of optics for incoherent operations with microwave electrodes could facilitate scaling approaches using microwave coherent manipulation^{26–28}. Finally, the precise ion positioning demonstrated here indicates the practicality of schemes using integrated optics’ ability to generate spatially structured fields¹².

Table 1 | Error budget

Error source	Infidelity ($\times 10^{-3}$)
Motional mode heating	2(1)
Motional frequency drifts	1
Laser frequency noise	1
Two-ion readout error	0.9
Kerr cross-coupling	0.4
Spectator mode occupancies	0.3
Spontaneous emission	0.03
Total	$\sim 6 \times 10^{-3}$

Error sources and estimated contributions to infidelity of the Bell states generated in this work.

of an ‘analysis’ $\pi/2$ pulse after the gate time $\tau_g = 66$ μs . The fit contrast (red line) of 0.992(2), together with the even populations measured at the gate time 0.994(1), indicate a Bell state generated with fidelity 0.993(2). In both **b** and **c**, each point represents an average over 200 experimental shots, with error bars indicating 1σ standard errors from projection noise.

Beyond their broad relevance in trapped-ion quantum information processing, these approaches may also benefit atomic clocks, whether in portable systems or in precise clocks using multiple trap zones⁶, as well as neutral-atom quantum systems³⁵.

Online content

Any methods, additional references, Nature Research reporting summaries, source data, extended data, supplementary information, acknowledgements, peer review information; details of author contributions and competing interests; and statements of data and code availability are available at <https://doi.org/10.1038/s41586-020-2823-6>.

1. Leibfried, D., Blatt, R., Monroe, C. & Wineland, D. Quantum dynamics of single trapped ions. *Rev. Mod. Phys.* **75**, 281–324 (2003).
2. Häffner, H., Roos, C. F. & Blatt, R. Quantum computing with trapped ions. *Phys. Rep.* **469**, 155–203 (2008).
3. Monroe, C. & Kim, J. Scaling the ion trap quantum processor. *Science* **339**, 1164–1169 (2013).
4. Mehta, K. K. et al. Integrated optical addressing of an ion qubit. *Nat. Nanotechnol.* **11**, 1066–1070 (2016).
5. Kielpinski, D., Monroe, C. & Wineland, D. J. Architecture for a large-scale ion-trap quantum computer. *Nature* **417**, 709–711 (2002).
6. Keller, J. et al. Controlling systematic frequency uncertainties at the 10^{-19} level in linear Coulomb crystals. *Phys. Rev. A* **99**, 013405 (2019).
7. Harty, T. et al. High-fidelity preparation, gates, memory, and readout of a trapped-ion quantum bit. *Phys. Rev. Lett.* **113**, 220501 (2014).
8. Ballance, C., Harty, T., Linke, N., Sepiol, M. & Lucas, D. High-fidelity quantum logic gates using trapped-ion hyperfine qubits. *Phys. Rev. Lett.* **117**, 060504 (2016).
9. Gaebler, J. P. et al. High-fidelity universal gate set for $^9\text{Be}^+$ ion qubits. *Phys. Rev. Lett.* **117**, 060505 (2016).
10. Fowler, A. G., Whiteside, A. C. & Hollenberg, L. C. Towards practical classical processing for the surface code. *Phys. Rev. Lett.* **108**, 180501 (2012).
11. Amini, J. M. et al. Toward scalable ion traps for quantum information processing. *New J. Phys.* **12**, 033031 (2010).
12. Mehta, K. K., Zhang, C., Miller, S. & Home, J. P. Towards fast and scalable trapped-ion quantum logic with integrated photonics. *Proc. SPIE* **10933**, 109330B (2019).
13. Wörhoff, K., Heideman, R. G., Leinse, A. & Hoekman, M. TriPLeX: a versatile dielectric photonic platform. *Adv. Opt. Technol.* **4**, 189–207 (2015).
14. Chiaverini, J. et al. Surface-electrode architecture for ion-trap quantum information processing. *Quantum Inf. Comput.* **5**, 419–439 (2005).
15. Mehta, K. et al. Ion traps fabricated in a CMOS foundry. *Appl. Phys. Lett.* **105**, 044103 (2014).
16. Schindler, P. et al. A quantum information processor with trapped ions. *New J. Phys.* **15**, 123012 (2013).
17. Mehta, K. K. & Ram, R. J. Precise and diffraction-limited waveguide-to-free-space focusing gratings. *Sci. Rep.* **7**, 2019 (2017).
18. Roos, C. et al. Experimental demonstration of ground state laser cooling with electromagnetically induced transparency. *Phys. Rev. Lett.* **85**, 5547–5550 (2000).
19. James, D. F. Quantum dynamics of cold trapped ions with application to quantum computation. *Appl. Phys. B* **66**, 181–190 (1998).
20. Wineland, D. J. et al. Experimental issues in coherent quantum-state manipulation of trapped atomic ions. *J. Res. Natl. Inst. Stand. Technol.* **103**, 259–328 (1998).

21. Brownnutt, M., Kumph, M., Rabl, P. & Blatt, R. Ion-trap measurements of electric-field noise near surfaces. *Rev. Mod. Phys.* **87**, 1419–1482 (2015).
22. Sørensen, A. & Mølmer, K. Entanglement and quantum computation with ions in thermal motion. *Phys. Rev. A* **62**, 022311 (2000).
23. Leibfried, D. et al. Experimental demonstration of a robust, high-fidelity geometric two ion-qubit phase gate. *Nature* **422**, 412–415 (2003).
24. Sedlacek, J. et al. Distance scaling of electric-field noise in a surface-electrode ion trap. *Phys. Rev. A* **97**, 020302 (2018).
25. Milne, A. R. et al. Phase-modulated entangling gates robust to static and time-varying errors. *Phys. Rev. Appl.* **13**, 024022 (2020).
26. Srinivas, R. et al. Trapped-ion spin-motion coupling with microwaves and a near-motional oscillating magnetic field gradient. *Phys. Rev. Lett.* **122**, 163201 (2019).
27. Harty, T. et al. High-fidelity trapped-ion quantum logic using near-field microwaves. *Phys. Rev. Lett.* **117**, 140501 (2016).
28. Zarantonello, G. et al. Robust and resource-efficient microwave near-field entangling $^9\text{Be}^+$ gate. *Phys. Rev. Lett.* **123**, 260503 (2019).
29. Debnath, S. et al. Demonstration of a small programmable quantum computer with atomic qubits. *Nature* **536**, 63–66 (2016).
30. Lindenfesler, F., Marinelli, M., Negnevitsky, V., Ragg, S. & Home, J. P. Cooling atomic ions with visible and infra-red light. *New J. Phys.* **19**, 063041 (2017).
31. West, G. N. et al. Low-loss integrated photonics for the blue and ultraviolet regime. *APL Photon.* **4**, 026101 (2019).
32. Niffenegger, R. J. et al. Integrated multi-wavelength control of an ion qubit. *Nature* <https://www.nature.com/articles/s41586-020-2811-x> (2020).
33. Kaufmann, H. et al. Scalable creation of long-lived multipartite entanglement. *Phys. Rev. Lett.* **119**, 150503 (2017).
34. Schäfer, V. et al. Fast quantum logic gates with trapped-ion qubits. *Nature* **555**, 75–78 (2018).
35. Saffman, M., Walker, T. G. & Mølmer, K. Quantum information with Rydberg atoms. *Rev. Mod. Phys.* **82**, 2313–2363 (2010).

Publisher's note Springer Nature remains neutral with regard to jurisdictional claims in published maps and institutional affiliations.

© The Author(s), under exclusive licence to Springer Nature Limited 2020

Methods

Device design and fabrication

Devices were designed similarly to those in previous work¹⁷. The grating designs exploit the reflection from the silicon substrate below to increase grating strength; a compromise between grating length and efficiency resulted in a designed radiation efficiency of 50% in these devices (defined as upwards-radiated power as a fraction of input power). Emission into a single grating order is ensured by choosing a sufficiently large grating wavenumber $\beta_g = \frac{2\pi}{\Lambda}$ (with Λ the grating period). The curvature of the grating lines is calculated to induce focusing along \hat{y} in Fig. 1b, with designed focusing limited to about 3- μm waists to relax sensitivity to misalignments in fabrication. Λ is constant over the grating length in these devices to generate an approximately collimated beam along the trap axis.

Mode overlap simulations predict a 1-dB coupling loss between an optical mode with 5.4- μm mode-field diameter and the waveguide mode of the 25-nm-thick SiN waveguides. Waveguides formed of the thin SiN core in the fibre coupling regions are strongly polarizing in our devices, in that owing to the metal and silicon a few micrometres from the core, only the mode with the *E*-field polarized predominantly along the horizontal in Fig. 2b propagates in these regions with low loss. Polarization is maintained in the high-confined waveguides due to the large index mismatch between the quasi-transverse-electric and quasi-transverse-magnetic modes in these regions, typical for integrated waveguides with non-square aspect ratios.

Grating designs were verified with three-dimensional (3D) finite-difference time-domain (FDTD) simulations (Lumerical FDTD Solutions), and 3D simulations of the ion-trap potentials were performed in COMSOL; designs were drawn in Cadence Virtuoso.

Various trap and optical designs were drawn on a $2.2 \times 2.2 \text{ cm}^2$ reticle repeated across a four-inch wafer (Extended Data Fig. 1). A design drawing of the trap die used in this work is shown in Extended Data Fig. 1c, together with a magnified view near one of the trap zones with 729-nm and 854/866-nm waveguides and gratings. The fabrication process used here allowed relative alignment between different layers within approximately $\pm 2 \mu\text{m}$, and the electron-beam grating lines were aligned within about 300 nm to the photolithographically defined waveguides. To account for possible misalignments, grating lines in zones 1 and 3 were intentionally offset along *y* by $\pm 300 \text{ nm}$. All three zones were characterized in optical measurements; the 300-nm offset between grating and waveguide features results in a roughly 2.5- μm beam shift along *y* at the ion height between zones, in accordance with simulations.

Fabrication was performed by LioniX International¹³. Devices were fabricated on silicon wafers with 5–10 $\Omega \text{ cm}$ resistivity; the bottom 2.7- μm oxide layer was formed via thermal oxidation, with the waveguides formed in low-pressure chemical vapour deposition SiN layers. Following combined stepper photolithography and electron-beam patterning of the waveguide/grating features, low-pressure chemical vapour deposition SiO_2 cladding was deposited. The platinum layer was then deposited after planarization, and patterned via contact photolithography ion beam etching. A thin (90 nm) Ta_2O_5 layer serves as an adhesion layer above the Pt. The upper plasma-enhanced chemical vapour deposition SiO_2 isolation was patterned to allow vias between the two metal layers, after which the upper gold was sputtered and patterned via contact photolithography and a liftoff procedure to form the trap electrodes.

Diced wafers were delivered to ETH, where die were characterized for optical performance, or else cleaned, packaged and fibre-attached for ion-trap experiments.

Assembly and fibre attachment

A standard eight-channel fibre V-groove array populated with Nufern S630-HP fibres spaced at 127- μm pitch was purchased from OZ Optics. Eight waveguides extend to the edge of the chip die to interface to

the array, with the outer two forming a simple loop structure used to align the array by maximizing loop transmission. Standard non-polarization-maintaining fibres are used in this work, and in-line fibre polarizers control the input polarization.

Individual trap dies were removed from the wafer, and a $1.5 \times 3.5 \text{ mm}^2$ SiO_2 piece of 500 μm thickness was epoxied (EPO-TEK silver epoxy, model H21D) to the top surface of the trap chip at the fibre-coupling edge (Extended Data Fig. 2, and visible near the fibre array in Fig. 1a). This piece was previously coated in 300-nm gold via electron-beam evaporation on faces exposed to the ion, to minimize possible stray fields. Subsequently the die was coated in a protective photoresist layer and mounted in a custom-machined holder for polishing on standard fibre polishing paper. Polishing reduces roughness and associated loss at the coupling interface, and introduces convex curvature to the facet, important for the fibre attachment as described below. The silicon substrate was scribed with a diamond scribe to break through the native oxide; after dissolving the protective photoresist and attaching the die to the carrier PCB, a drop of silver epoxy was applied both to contact the silicon substrate to the ground on the carrier PCB, as well as to ensure grounding of the metal on the SiO_2 piece near the fibre array. The trap electrodes were then wirebonded to the contacts on the carrier PCB.

To attach the fibre array, the facet-polished and wirebonded sample was mounted on a temperature-controlled chuck fixed to a three-axis tip/tilt/rotation stage and raised to 95 °C. The fibre array, held in a custom machined stainless-steel mount in a three-axis translation stage, was then aligned and pressed against the chip in such a fashion that static friction between the two interfaces allowed coupling to be passively maintained for hours (see Extended Data Fig. 2a for a schematic of this interface). Low-temperature curing, non-transparent, filled epoxy (EPO-TEK T7109-19) was then dropped at the two edges and allowed to wick into the gap; this epoxy was chosen as its flexibility should result in robustness to temperature changes. The convex curvature of the trap die at this interface ensures that the epoxy does not interact with the optical mode, allowing choice of mechanically suitable epoxies without restriction to transparent variants; minimizing exposure of the optical mode to the epoxy is also important in avoiding possible photo-effects, which can be problematic even with transparent adhesives exposed to visible wavelengths. The total contact area used for the attachment is about $1.0 \times 3.5 \text{ mm}^2$. After a few hours of curing with the sample stage at 95 °C, the holder for the fibre array was loosened to allow the fibre array to move with the trap chip, the sample stage was cooled to room temperature and no drop in transmission was observed. We have performed three attachments in this fashion so far, and found all robust to temperature drops. We note that in this work, the epoxy was applied manually—more precise automatic dispensing should allow more symmetric application, which may increase robustness to temperature changes further still.

The transmission of a single fibre-waveguide interface was measured at various wavelengths within the bandwidth of a continuous-wave titanium:sapphire laser, measuring the transmission from input fibre 1 to fibre 8 and subtracting the measured waveguide loss. The broadband nature of this coupling is shown in the measurements in Extended Data Fig. 2b. On applying current to a heater on the carrier PCB near the chip and then cooling the assembly to 7 K, we observed a small increase in loss from 1.4 dB to 2.4 dB at 729 nm, but saw no further changes after two additional temperature cycles between room temperature and 7 K. These coupling losses compare favourably to previous published work on cryogenic fibre attachment³⁶. This method furthermore allows multiple channels aligned in parallel, and at shorter wavelengths with more demanding alignment tolerances.

Waveguide/grating characterization and optical losses

Structures consisting of waveguides of varying length on chip were included on the reticle design to measure waveguide losses in the high-confinement mode used for routing on chip. These were

measured to be 2 dB cm^{-1} at 729 nm, and verified with measurements of quality factors of ring resonators also included in the design. Wavelength-dependent losses were measured from 729 nm to 920 nm using a tunable continuous-wave titanium:sapphire source; we observe a reduction in loss as a function of increasing wavelength consistent with scattering from sidewall roughness being the dominant contribution. We therefore expect improved lithography to reduce this propagation loss.

Grating emission was profiled (Fig. 2c–e) using a microscope mounted on a vertical translation stage to image the emission at various heights above the chip¹⁷ onto a scientific charge-coupled device camera (Lumenera Infinity 3S-1UR), through a 0.95-numerical-aperture objective (Olympus MPLANAPO50x). An RF modulation input was applied to the current drive of a 730-nm diode laser to reduce the coherence length to avoid reflection artefacts in the imaging system. The measured height of the beam focus above the top metal layer agrees with the FDTD simulation to within the measurement accuracy of about $2 \mu\text{m}$, and the measured emission angle in the x – z plane (Fig. 2d) matches design to within about 1° . These measurements are conducted at room temperature; considering the thermo-optic coefficients of SiO_2 and SiN ³⁷, we expect a change in emission angle on cooling to 7 K of roughly 0.2° , negligible in our geometry.

With 1.5 mW of 729-nm light input to the fibre outside the cryostat, we observe a $2.6\text{-}\mu\text{s}$ π -time, which is within 25% of the $2.0 \mu\text{s}$ predicted from a first-principles calculation¹⁹ accounting for the measured beam profile, and the total expected loss of 6.4 dB, arising from: 2.4 dB of fibre–chip coupling, 1 dB of waveguide loss over the 5-mm path length and 3 dB of grating emission loss. In the π -time calculation, we assume that the ion sits at the maximum of the $3.7\text{-}\mu\text{m}$ -beam waist along \hat{y} , resulting in a lower-bound given the micrometre-scale misalignments in these devices. Similar π -times are observed in the two-ion Rabi oscillations in Fig. 3a; we note that in this data, the $P_{\uparrow\downarrow\uparrow\downarrow}$ points are particularly helpful in bounding the Rabi frequency imbalance between the two ions, as a small imbalance results in these populations increasing substantially above 0.5 for pulses much longer than the π -time.

In testing power handling of these waveguides, a maximum of 300 mW was coupled into the single-mode waveguides at $\lambda = 729 \text{ nm}$; we did not observe damage to the waveguides from these intensities. Future work will investigate power handling limits and self-phase modulation in such waveguides at visible wavelengths, relevant to large-scale architectures with power for multiple zones input to a single bus waveguide.

Laser/cryogenic apparatus and trap operation

Diode lasers supply the various wavelengths used in the ion experiments. The 729-nm light used for coherent qubit control is stabilized to a high-finesse reference cavity resulting in a linewidth of order 100 Hz. Light transmitted through the cavity injection-locks a secondary diode, whose output passes through a tapered amplifier to a free-space double-pass acousto-optic modulator (AOM) setup for switching and frequency tuning, and subsequently a single-pass fibre-coupled AOM for pulse shaping. Two tones are applied to this fibre AOM also for generating the two sidebands in the MS gate. In the current experimental path, light propagates along approximately 9 m of fibre before and inside the cryostat on which acoustic noise is not actively cancelled; vibrations along this length of fibre contribute to the coherence decay presented below (Extended Data Fig. 3).

Though the photonics are functional at room temperature and the ion trap could be operated in ultrahigh vacuum without cryogenic cooling, we perform ion experiments in a cryogenic environment because of the ease of achieving low background pressure via cryopumping, the possibility for rapid trap installation/replacement (about two days), elimination of the need for baking of in-vacuum components and potentially reduced E -field noise near surfaces. The cryogenic apparatus used for ion-trap experiments is similar to that described previously³⁸.

Ions are loaded from neutral atom flux from a resistively heated oven within the 4-K chamber, followed by two-step photoionization using beams at 423 nm and 389 nm (ref. ³⁹). The fibre feedthrough consists simply of bare $250\text{-}\mu\text{m}$ -diameter acrylate-coated fibres epoxied (Stycast 2850FT) into a hole drilled in a CF blank flange mounted on the outer vacuum chamber. In the experiments presented in this paper, only the 729-nm beam for qubit control was delivered via integrated optics. Though waveguide structures for 854-nm/866-nm light were included on chip, these beams were routed together with the shorter wavelengths and delivered along conventional free-space beam paths for convenience given the previously existing optical setup.

The d.c. voltage sets for axial confinement, stray-field compensation and radial mode rotation were calculated using methods similar to those described in ref. ⁴⁰, based on 3D field simulations including the effect of exposed dielectric in our design.

We used these voltage sets to compensate stray fields in 3D by minimizing first and second micromotion sidebands of ion motion using two separate 729-nm beam paths. Light emitted by the grating has a wavevector $\mathbf{k}_g = k_0(\hat{z}\cos\theta_g + \hat{x}\sin\theta_g)$, where $\theta_g = 36^\circ$ is the emission angle from vertical and $k_0 = 2\pi/\lambda$ is the free-space wavenumber; this beam hence allows detection of micromotion along \hat{x} and \hat{z} . To compensate with sensitivity along \hat{y} , we used a second beam propagating in free-space along $\mathbf{k}_f = k_0(\hat{x}\cos\theta_f + \hat{y}\sin\theta_f)$ with $\theta_f = 45^\circ$. The calculated compensation voltage sets were used to minimize micromotion sidebands on both beam paths, which allowed us to achieve first micromotion sideband to carrier Rabi frequency ratios of $\Omega_{\text{MM}}/\Omega_{\text{car}} \approx 0.01$. Compensation fields applied are of the order 300 V m^{-1} along \hat{y} and $1,500 \text{ V m}^{-1}$ along \hat{z} ; day-to-day drifts are of the order 1%. We note the requirement for beams along two different directions for compensation arises from the typical assumption that the optical field's gradient (or, for quadrupole transitions, curvature) is non-zero along only its propagation direction; this does not hold for transverse focusing to wavelength-scale spots, in which ions undergoing micromotion perpendicular to the beam propagation direction will experience amplitude modulation. Beams focused to wavelength-scale spots may thus allow sensitivity to micromotion along multiple dimensions using a single beam.

The silicon partially exposed to the ion due to openings in the ground plane near the gratings was a potential concern, as previous work has seen that unshielded semiconductor can be problematic for stable trap operation¹⁵; we note that the substrate was not highly conductive or grounded in that previous work, and the grounding implemented here may be a notable difference. We have observed charging effects that appear to be related to carrier dynamics in the silicon; in particular, we observe jumps in the motional frequency of the order 10 kHz after Doppler cooling and state preparation with the 397-nm beam, which relax on millisecond timescales. These jumps were eliminated when a few milliwatts of infrared light were input into any of the waveguide channels on the chip. We attribute this to photoexcited carriers in the silicon from light scattered out of the waveguides and gratings, which diffuse through the substrate, increasing its conductivity and more effectively shorting it to ground, thereby suppressing stray fields originating from the substrate. The gate data taken in this paper were obtained with 4 mW of continuous-wave light at $\lambda = 785 \text{ nm}$ combined with the 729-nm pulses in the fibre coupled to input 3. It is possible that the use of heavily doped silicon would attenuate possible stray fields from the silicon; in a complementary metal–oxide–semiconductor context, highly doped and contacted layers at the exposed surfaces could potentially be used for the same purpose.

In addition, we observed kilohertz-level drifts in motional frequencies that relaxed on longer timescales of many minutes, which we attribute to charges trapped in or on the surface of the dielectric near the grating windows—this charging was clearly correlated, for example, to the 729-nm beams used for the MS gates being turned on. To minimize drifts in the motional frequency, we pulsed on the 729-nm beam during

Article

the 1-ms-long Doppler cooling pulse applied in each experimental shot, which together with the 785-nm light sent to the same coupler, led to a more constant optical flux through the opening and reduced these drifts to the level of a few hundred hertz. We additionally recalibrate the motional frequency every 15 s during MS gate experiments to minimize the effect of these remaining drifts. Our experiments serve as a baseline for performance achievable with no shielding of the exposed dielectric; the extent to which conductive shielding of this exposed dielectric (as recently demonstrated³²) reduces the magnitude of these effects will be an interesting question for future experiments.

Contributions to Bell-state infidelity and routes to improvement

Here we detail the error sources contributing to the Bell-state infidelity achieved via the integrated MS gate (Table 1) and discuss routes to improvement.

The heating rate of the two-ion stretch mode at 2.2 MHz used for the MS gates was measured to be $\dot{n} = 60(30)$ quanta per second, via fits to sideband flopping following variable wait times. For the single-loop gates implemented here, this contributes an error $\epsilon_h = \dot{n}\tau_g/2$ (ref. ⁴¹), resulting in our estimate of $2(1) \times 10^{-3}$. We measure a heating rate for a single-ion axial mode at 1.2 MHz of about 3,000 quanta per second, indicating E -field noise in our device about 100 times higher than in other cryogenic surface-electrode traps with a similar ion–electrode distance²⁴.

During gate experiments, we observed an average drift in motional frequency of 200 Hz magnitude between each recalibration. Assuming a linear drift in frequency between these calibration points, we generate a probability density function for the motional frequency error during each experimental shot, which together with simulated infidelity resulting from an error in gate detuning δ results in an expectation value for infidelity of 1×10^{-3} .

Spin coherence was assessed by means of Ramsey measurements on single qubits. Ramsey decays (Extended Data Fig. 3) observed when driving the $|S_{1/2}, m_j = -1/2\rangle$ to $|D_{5/2}, m_j = -1/2\rangle$ qubit transition through the integrated gratings were fitted by a model with a discrete noise component⁴² corresponding to oscillations in apparent carrier frequency occurring with 175-Hz periodicity, with a carrier frequency excursion amplitude of $2\pi \times 160$ Hz, together with a slower Gaussian decay with 1/e time of 11 ms. We found similar decays on the $|S_{1/2}, m_j = -1/2\rangle$ to $|D_{5/2}, m_j = -3/2\rangle$ transition, which has a two times higher magnetic field sensitivity, suggesting that laser frequency fluctuations (and not magnetic field drifts) are the dominant contribution. We estimate the infidelity resulting from the discrete noise component that dominates the Ramsey decay as follows. We perform numerical simulation to find the MS gate infidelity resulting from an offset carrier frequency, and average over the probability density function describing the offset during each shot for sinusoidal noise with the amplitude inferred from the Ramsey data. This results in an expectation value for infidelity of 1×10^{-3} , which serves as a lower bound for error as we have considered only the dominant noise component. We note that errors from drifts in both motional and carrier frequencies, together accounting for about 2×10^{-3} of our Bell-state infidelity, can add coherently in sequences of multiple gates.

The use of the stretch mode is advantageous with respect to heating, but introduces sensitivity to radial mode temperatures; variance in occupancy of the ‘rocking’ radial modes results in variance in the stretch mode frequency through a Kerr-type interaction^{43,44}. In our experiments, for technical reasons owing to beam directions required for EIT cooling, radial modes are not ground-state cooled, and after Doppler cooling we observe occupancies corresponding to $\bar{n} \approx 12 - 13$ for the modes at 3.5 MHz and $\bar{n} \approx 5$ for those at 5.5 MHz; these result in an estimate of the resulting infidelity of 4×10^{-4} .

The warm radial modes also contribute to shot-to-shot carrier Rabi frequency fluctuations, as the grating beam couples to all radial modes

(these dominate the decay observed in Rabi oscillations in Fig. 3a, Extended Data Fig. 5a). From the same occupancies given above, we estimate an infidelity of 3×10^{-4} .

Qubit-state preparation is based on frequency-selected optical pumping on the quadrupole transition (repeatedly driving a 729-nm π -pulse starting from $|S_{1/2}, m_j = +1/2\rangle$ and repumping with the 854-nm beam to the fast-decaying $P_{3/2}$ levels); we measure preparation of qubits in the starting $|S_{1/2}, m_j = -1/2\rangle$ state with infidelities $< 10^{-4}$. Qubit-state detection is based on applying a resonant 397-nm pulse (driving $S_{1/2} \leftrightarrow P_{1/2}$ transitions) for 250 μ s after each shot and thresholding the number of photon counts detected by our photomultiplier tube, to infer whether the detection event corresponded to 0, 1 or 2 ions bright. The 1-bright-ion histogram is well separated from the dark distribution and contributes negligible error; however, with the optimal threshold, 0.09% of 1-bright-ion events are mistaken for 2 bright, and vice versa, contributing 0.9×10^{-4} to our Bell-state infidelity (see Extended Data Fig. 4 for two-ion readout histograms).

The gate pulse is smoothly ramped on and off over about 5 μ s, which reduces infidelity from off-resonant excitation of the direct drive term in the MS interaction Hamiltonian²² to negligible levels for these gate times.

The effects summarized above together account for about 0.6% infidelity. The gate fidelity could clearly be increased by means of certain technical improvements; error from motional mode heating can be suppressed by two orders of magnitude if improved trap materials or technical noise sources can allow heating rates comparable to the lowest-noise cryogenic surface traps²⁴. Shielding of the exposed dielectric, for example, with a transparent conductor³² or perhaps with thin, semitransparent metal films, should reduce motional frequency drifts, and optimal strategies for this are likely to be essential, especially for trap chips delivering high powers in the blue/ultraviolet as well. Laser noise could be reduced using improved implementation of acoustic noise cancellation on optical fibre in our system⁴⁵, together with technical improvements to our laser-frequency stabilization. Ground-state cooling of radial modes can suppress Kerr cross-coupling and Rabi frequency fluctuations from radial mode occupancies, both of which contribute error roughly quadratic in \bar{n} , by a factor of 100. Couplers and beam/field geometries in future chips for EIT ground-state cooling of all modes⁴⁶ will be an enabling development. Aside from these possible technical improvements, multi-loop and composite-pulse gate implementations can reduce infidelity from motional heating and frequency drifts, as well as laser-frequency drifts²⁵. Our current experiments show no obvious limit to fidelity arising from optical integration, and it appears such implementations may assist in approaching the $\sim 10^{-5}$ limit imposed by spontaneous emission for typical gate times using this qubit.

Cross-talk between trap zones

Optical radiation brings advantages in the possibility for tight beam focuses addressing individual ions or ensembles within larger systems.

We quantified cross-talk levels expected in parallel operation of multiple zones in the present device by inputting light to adjacent fibre couplers and measuring the effect on the ion in the experimental trap zone 3 (zones and waveguide inputs labelled in Extended Data Fig. 1c). Extended Data Fig. 5a shows Rabi flopping observed on a single ion trapped in zone 3 with light coupled to input 3 (which directly feeds the grating addressing this zone). Light intended to address zone 2 would instead be coupled to input 5; when we send the same optical power to input 5, we observe Rabi oscillations with a 1,000 times lower Rabi frequency on the ion in zone 3 (Extended Data Fig. 5b), indicating a relative intensity in this non-addressed zone of ~ 60 dB.

This level of cross-talk appears to arise from a combination of coupling between the waveguides on-chip (that is, coupling from the waveguide of input 5 to input 3, and then emission by the grating in zone 3) and weak sidelobes of emission from the zone 2 grating to the

ion in zone 3. Similar levels of cross-talk at –60 dB are observable when feeding in light to input 1, which propagates in a loop around the device and to no grating. The beam profile emitted in this case is probed by measuring ion response at different ion positions along the trap axis and is observed to be consistent with that emitted by the 729-nm coupler in zone 3; hence, we attribute this cross-talk to coupling between the waveguides fed by input 1 and input 3. Furthermore, when polarization is adjusted to minimize transmission to the loop output, the cross-talk drops by 20 dB, suggesting that the bulk of cross-talk into the zone 3 coupler comes from inter-waveguide coupling rather than scatter at the fibre–chip interface. We expect lower-loss waveguides with less sidewall scattering to reduce this effect. Cross-talk from the emission of the grating itself is particularly pronounced along the axial direction we probe here¹⁷, and we expect optimized arrangements and designs to reduce this as well. A variety of composite pulse schemes can reduce the impact of coherent errors resulting from such cross-talk.

Hybrid Zeeman/optical qubit encoding

Sequences of gates conducted using the optical qubit addressed in this work would require phase stability of the driving 729-nm light over the entire algorithm, a challenging technical requirement for algorithms extending beyond many seconds. The 1.1-s spontaneous emission lifetime also limits memory time achievable with this transition.

We note that both issues may be ameliorated by hybrid approaches where, for example, in $^{40}\text{Ca}^+$, qubits can be stored in the two $S_{1/2}$ Zeeman sublevels (and single-qubit gates implemented via RF magnetic fields), with excitation from one sublevel to the $D_{5/2}$ state only to implement two-qubit interactions.

For each ion, we denote the three levels involved $|0\rangle = |S_{1/2}, m_j = -1/2\rangle$, $|1\rangle = |S_{1/2}, m_j = +1/2\rangle$ and $|2\rangle$ a sublevel of the $D_{5/2}$ manifold; $|0\rangle$ and $|1\rangle$ represent the long-term ‘memory’ qubit. $|1\rangle$ is mapped to $|2\rangle$ for optical multi-qubit gates via rotations $\hat{R}_{12}(\pi, \phi) = \exp(-i\pi\hat{\sigma}_{12}\phi/2)$, with $\hat{\sigma}_{12}(\phi) = \hat{\sigma}_{x12}\cos\phi + \hat{\sigma}_{y12}\sin\phi$, where $\hat{\sigma}_{x12}$ and $\hat{\sigma}_{y12}$ are Pauli matrices for states $|1\rangle$ and $|2\rangle$. The MS interaction $\hat{U}_{02}^{\text{MS}}(\phi)$ between $|0\rangle$ and $|2\rangle$ is expressed exactly as in the main text, with Pauli matrices appropriate to these two levels; defining the global π -rotation on qubits a and b as $\hat{R}_{12}(\phi) = \hat{R}_{12}(\pi, \phi)_a \otimes \hat{R}_{12}(\pi, \phi)_b$, we find the total unitary $\hat{R}_{12}(\phi)\hat{U}_{02}^{\text{MS}}(\phi)\hat{R}_{12}(\phi)$ is independent of the constant laser phase offset ϕ . In fact, we note this is not unique to the MS gate and would apply to any optically implemented unitary.

Such an approach may allow systems to exploit the relatively low power requirements and high addressability of optical interactions, while benefiting from the long memory times and relaxed laser-phase stability requirements of microwave qubits.

Data availability

The raw data generated during this study are available from the corresponding author on reasonable request.

Code availability

The analysis code employed in this study is available from the corresponding author on reasonable request.

36. McKenna, T. P. et al. Cryogenic packaging of an optomechanical crystal. *Opt. Express* **27**, 28782–28791 (2019).
37. Elshaari, A. W., Zadeh, I. E., Jöns, K. D. & Zwiller, V. Thermo-optic characterization of silicon nitride resonators for cryogenic photonic circuits. *IEEE Photon. J.* **8**, 2701009 (2016).
38. Leupold, F. M. *Bang-bang Control of a Trapped-Ion Oscillator*. PhD thesis, ETH Zurich (2015).
39. Lucas, D. et al. Isotope-selective photoionization for calcium ion trapping. *Phys. Rev. A* **69**, 012711 (2004).
40. Allcock, D. et al. Implementation of a symmetric surface-electrode ion trap with field compensation using a modulated Raman effect. *New J. Phys.* **12**, 053026 (2010).
41. Ballance, C. J. *High-fidelity Quantum Logic in Ca^+* . PhD thesis, Oxford Univ. (2017).
42. Kotler, S., Akerman, N., Glickman, Y. & Ozeri, R. Nonlinear single-spin spectrum analyzer. *Phys. Rev. Lett.* **110**, 110503 (2013).
43. Roos, C. et al. Nonlinear coupling of continuous variables at the single quantum level. *Phys. Rev. A* **77**, 040302 (2008).
44. Nie, X. R., Roos, C. F. & James, D. F. Theory of cross phase modulation for the vibrational modes of trapped ions. *Phys. Lett. A* **373**, 422–425 (2009).
45. Ma, L.-S., Jungner, P., Ye, J. & Hall, J. L. Delivering the same optical frequency at two places: accurate cancellation of phase noise introduced by an optical fiber or other time-varying path. *Opt. Lett.* **19**, 1777–1779 (1994).
46. Lechner, R. et al. Electromagnetically-induced-transparency ground-state cooling of long ion strings. *Phys. Rev. A* **93**, 053401 (2016).

Acknowledgements We thank D. Marchenko, D. Geuzebroek and A. Leinse at LioniX International for fabrication of the devices and for discussions during design; V. Negnevitsky and Matteo Marinelli for their work on the experimental control system and software used for these experiments; S. Miller for assistance in characterization of fabricated photonic devices; F. Gürkaynak at ETH for support with CAD software; the ETH FIRST cleanroom staff; and E. Schlatter for helpful advice on epoxies. We acknowledge funding from the Swiss National Fund grant number 200020165555, NCCR QSIT, ETH Zürich, the EU Quantum Flagship, and an ETH Postdoctoral Fellowship.

Author contributions K.K.M. conceived the work, and designed, characterized and assembled the trap devices. K.K.M., C.Z. and M.M. performed the trapped-ion experiments in an apparatus with substantial contributions from C.Z., M.M., T.-L.N. and M.S. KKM analysed the data. J.P.H. supervised the work, and K.K.M. wrote the manuscript with input from all authors.

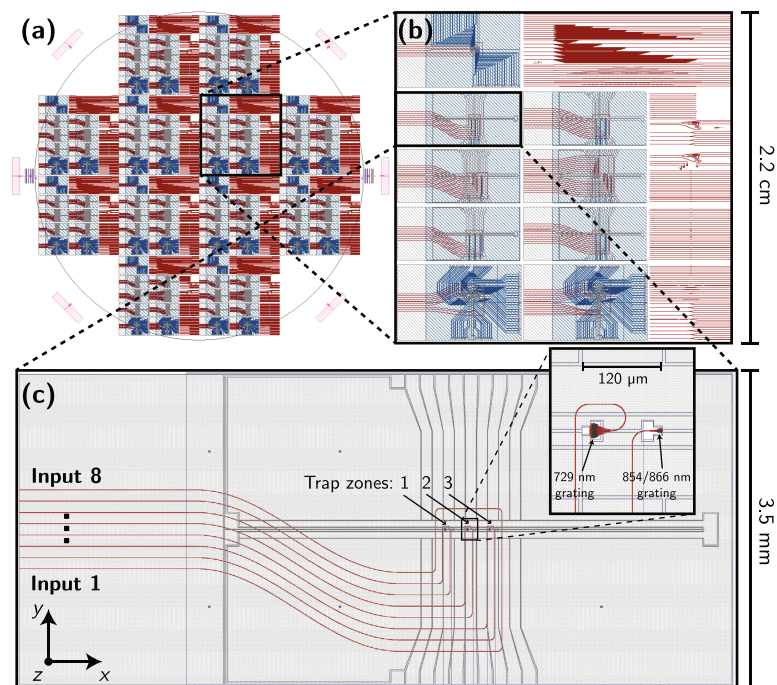
Competing interests The authors declare no competing interests.

Additional information

Correspondence and requests for materials should be addressed to K.K.M.

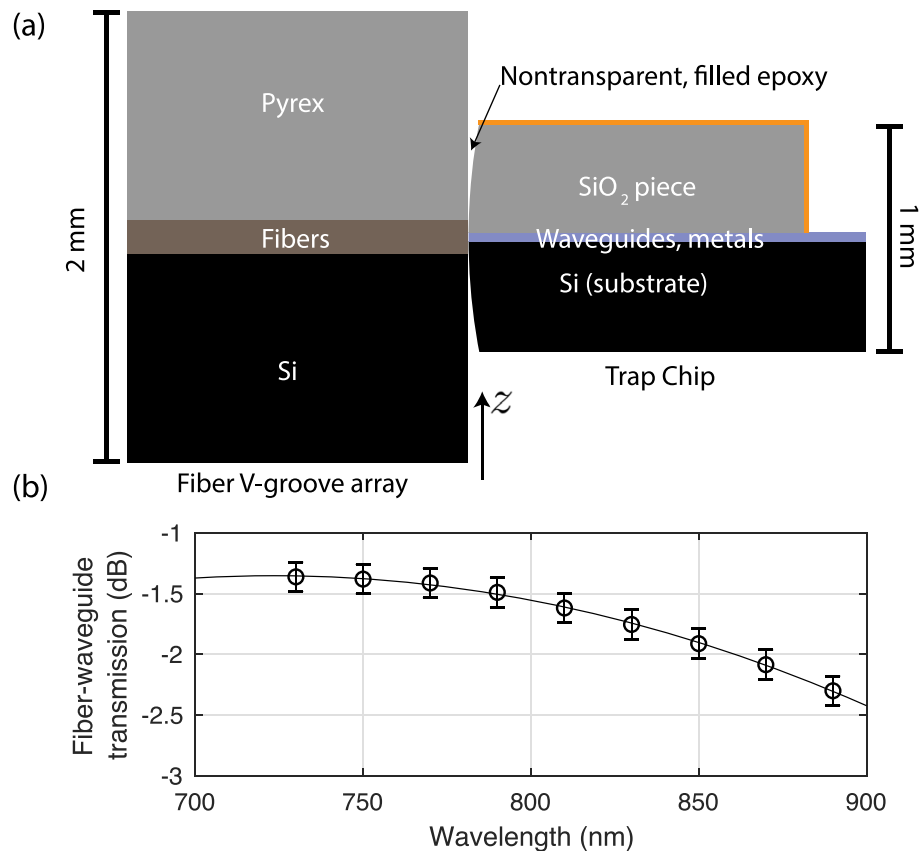
Peer review information *Nature* thanks Jungsang Kim and the other, anonymous, reviewer(s) for their contribution to the peer review of this work.

Reprints and permissions information is available at <http://www.nature.com/reprints>.

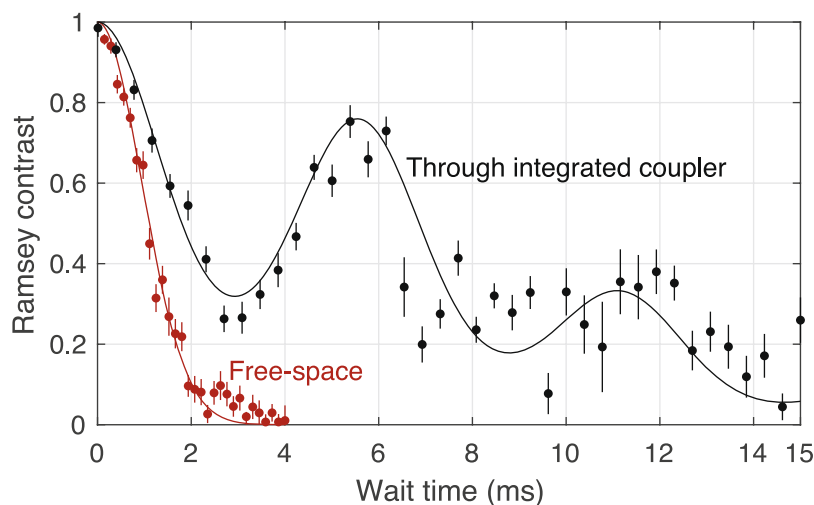


Extended Data Fig. 1 | Design layout. **a**, Mask images for device fabrication across a four-inch wafer. **b**, Individual $2.2 \times 2.2 \text{ cm}^2$ reticle, showing trap designs as well as independent optics test structures. **c**, Trap design used in ion experiments presented here. In all images, SiN features are shown in red,

the top trap electrode layer in grey and the ground plane in blue. The eight waveguides coupled to the fibre array are labelled at the left, with inputs 1 and 8 forming a loop structure used to align the fibre V-groove array.

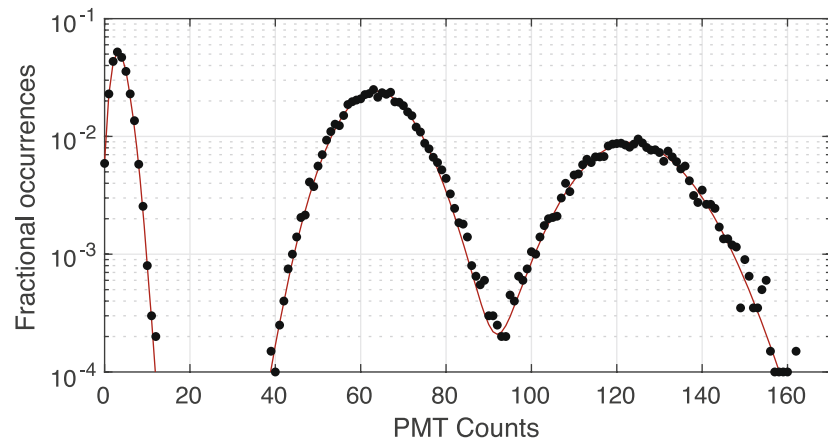


Extended Data Fig. 2 | Fibre attachment. Fibre attachment process schematic and measured single-pass fibre-waveguide coupling losses inferred from a loop-back structure on-chip; solid line is a guide to the eye.



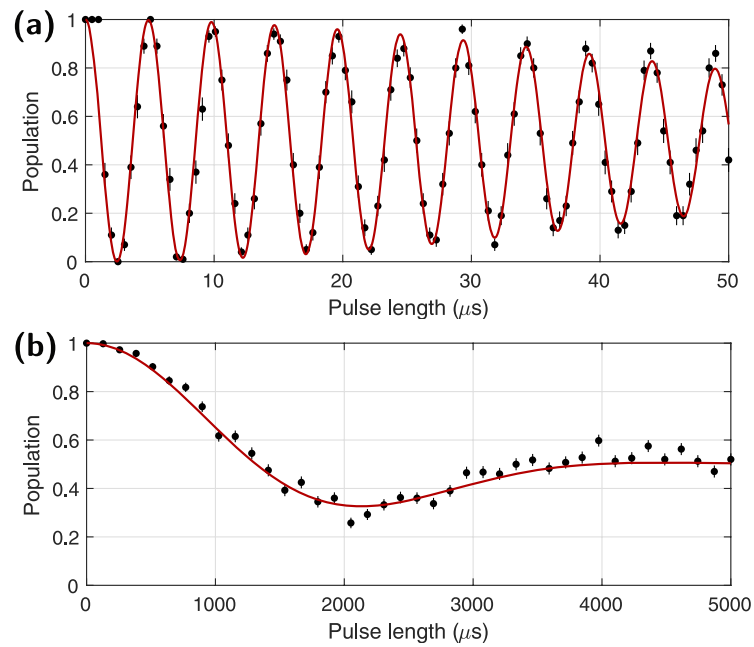
Extended Data Fig. 3 | Ramsey coherence measurements. We apply two $\pi/2$ pulses separated by a variable wait time, and the fringe contrast on scanning the phase of the second pulse relative to the first is plotted to assess T_2^* . Data are shown using the same light guided through the in-cryostat fibres and integrated couplers (black points and fit) or through free space (red points and fit). The fit to the data observed with the integrated coupler was used to infer

laser noise parameters relevant to gate infidelity calculation; the observation of markedly faster decoherence when driving with the free-space beam (red points/fit) using the same 729-nm source indicates the integrated beam path's advantage in insensitivity to cryostat vibrations. Error bars on points represent 68% confidence intervals on fit contrasts.



Extended Data Fig. 4 | Readout histograms. Histogram of photomultiplier tube (PMT) counts observed in detection events over all points in the parity scan of Fig. 4, fitted to a sum of three Poissonian distributions.

Each distribution corresponds to counts obtained during a 250- μ s detection period from events with either 0, 1 or 2 ions in the bright state.



Extended Data Fig. 5 | Cross-talk characterization. a, b, Rabi oscillations at zone 3 with light coupled to the port directly addressing this zone (input 3) (**a**), and with light coupled to the port intended to address zone 2 (input 5) (**b**).

Fits to Rabi oscillations with a Gaussian envelope decay indicate π -times of 2.4 μs (**a**) and 2.6 ms (**b**).